

# Semi-Empirical Prediction of Noise from Non-Zero Pressure Gradient Turbulent Boundary Layers

Steven A. E. Miller\*

*University of Florida*

Turbulent boundary layers with non-zero pressure gradients are present on almost all aerospace flight vehicles and radiate acoustic waves. A semi-empirical mathematical model is developed to predict acoustic radiation from non-zero pressure gradient turbulent boundary layers. The arguments of the mathematical model are the turbulent statistics and meanflow, which are numerically derived from steady Reynolds-averaged Navier-Stokes equations closed by an algebraic Reynolds stress model. Predictions are conducted for four subsonic Mach numbers and five non-dimensional pressure gradients. The turbulent statistics and meanflow relative to the zero pressure gradient boundary layer are quantified. Predictions of acoustic radiation are compared with a previously developed analytical model and a well validated large eddy simulation. Finally, relative changes of the power spectra for four Mach numbers and four non-dimensional pressure gradients are compared with corresponding zero-pressure gradient flows.

## Nomenclature

Symbols		Greek Symbols	
$A_{ijlm}$	Coefficient matrix	$\Delta_1$	Parameter of integration
$c$	Speed of sound	$\delta$	Boundary layer thickness
$c_f$	Skin friction	$\delta_{ij}$	Kronecker delta function
$c_i$	Constants	$\boldsymbol{\eta}$	Vector between sources
$F_t$	Far-field term	$\eta$	Cross-stream source separation
$f$	Frequency	$\Pi$	Coles wake factor
$G$	Cross-power spectral density	$\xi$	Streamwise source separation
$\mathcal{L}_\tau$	Integrated terms with respect to $\tau^{th}$ derivative	$\kappa$	Von Karman constant
$k$	Turbulent kinetic energy	$\rho$	Density
$l_{si}$	Turbulent length scale in direction $i$	$\rho_w$	Density at wall
$M_t$	Mid-field term	$\tau$	Retarded time
$N_t$	Near-field term	$\tau_s$	Turbulent time scale
$\mathbf{R}_{ijlm}$	Model of two-point cross-correlation of Lighthill stress tensor	$\tau_w$	Wall shear stress
$R$	Normalized two-point cross-correlation	$\nu$	Kinematic viscosity
$R_c$	Recovery factor	$\zeta$	Spanwise source separation
$\mathbf{r}$	Vector from source to observer	$\omega$	Radial frequency
$S$	Auto-power spectral density		
$t$	Observer time	Non-Dimensional Numbers	
$T_{ij}$	Lighthill stress tensor	$\mathcal{M}$	Vector Mach number
$T$	Temperature	$Re$	Reynolds number
$\mathbf{u}$	Fluid velocity	$Re_{Kp}$	Porous Reynolds number
$\mathbf{x}_i$	Observer position	$St$	Strouhal number
$u_\tau$	Wall friction velocity		
$V$	Volume that boundary layer encompasses	Abbreviations	
$x_t$	Streamwise location of velocity profile from leading edge	CPSD	Cross-power spectral density
$u^+$	Velocity coordinate	CSAA	Cross-spectral acoustic analogy
$\mathbf{y}_i$	Source position	DNS	Direct numerical simulation
$y^+$	Wall coordinate	LES	Large eddy simulation
		PIV	Particle image velocimetry
		SPL	Sound pressure level

---

\*Assistant Professor, Mechanical and Aerospace Engineering, University of Florida, P.O. Box 116250, Gainesville, FL, 32611, USA, AIAA Senior Member, saem@ufl.edu or saemiller@gmail.com

## Introduction

Most industrial flows contain strong adverse or favorable pressure gradients in the axial direction within the turbulent boundary layer. Early investigations of turbulent boundary layers started because of the 1904 lecture by Prandtl.<sup>1</sup> Articles of Kovasznay,<sup>2</sup> Kline et al.,<sup>3</sup> Eichelbrenner,<sup>4</sup> and Schlichting<sup>5</sup> summarize the process of the dynamics of turbulence within the boundary layer. In this paper, we predict the acoustic radiation from a non-zero pressure gradient turbulent boundary layer.

Excellent investigations that focus on the statistics of turbulence within turbulent boundary layers with non-zero pressure gradient are rare. Similarity solutions for the scaling of statistics within the turbulent boundary layer remain an open canonical problem. In the review article of Kovasznay,<sup>2</sup> he characterizes the pressure gradient using a non-dimensional approach,  $K = \nu(\rho u_\infty^3)^{-1} \partial p / \partial x$ , where  $K$  is the non-dimensional pressure gradient,  $p$  is the pressure,  $u$  is the streamwise velocity component,  $x$  is the axial direction,  $\rho$  is the density, and  $\nu$  is the viscosity. Kline et al.<sup>3</sup> examined mean velocity profiles of various boundary layers characterized by  $K$ . Boundary layers with a mild pressure gradient are nearly in equilibrium. For large values of  $K$  the boundary layer is not in equilibrium. Kline et al.<sup>3</sup> showed that the boundary layer velocity profile possesses similarity within the outer region when normalized with shear velocity and possesses similarity within the inner region when normalized by wall friction velocity,  $u_\tau$ . Thus, it is difficult to propose a composite profile like that shown previously which explicitly accounts for variation of  $K$ . Castillo,<sup>6</sup> who collapsed the meanflow for pipes and channel flows using power laws instead of log laws, showed that collapse of boundary layers in pressure gradients could be possible. This latter approach opens the possibility of correctly predicting the boundary layer meanflow with a pressure gradient. It does not yield any insight on the effect of the boundary layer pressure gradient on the turbulence statistics.

The first model for the prediction of noise from turbulent boundary layers was of Powell.<sup>7</sup> Powell<sup>7</sup> used Lighthill's acoustic analogy in conjunction with a mirror source and showed that the acoustic power is proportional to the volumetric integral of the second time derivative of the Lighthill stress tensor multiplied by  $\rho_\infty^{-1} c_\infty^{-5}$ . Analysis of Powell<sup>7</sup> shows that pressures on the wall are only the aerodynamic 'imprint' of turbulence, and the recent work of Naka et al.<sup>8</sup> supports this viewpoint. In a series of philosophical papers, Ffowcs Williams<sup>9,10</sup> and Ffowcs Williams and Purshouse<sup>11</sup> examined the noise due to turbulent boundary layers. No predictions are shown within these papers, thus it is difficult to justify the validity of their theories. As the pressure on the wall is an imprint of the large-scale turbulence within the boundary layer, it is tempting to create a prediction model for the acoustic radiation that is dependent on the wall wavenumber pressure spectrum. An empirical approach of Howe<sup>12</sup> related the wall wavenumber pressure spectrum to the acoustic spectrum. Similar to the model of Howe,<sup>12</sup> Glegg et al.<sup>13</sup> created a model that depends on the wavenumber spectrum of the surface pressure fluctuations, and additionally included a correlation function for the surface roughness distribution. Numerically based approaches include those of Hu et al.,<sup>14,15</sup> who performed a direct numerical simulation (DNS) combined with an acoustic analogy and a half-space Green's function. Gloerfelt and Berland<sup>16</sup> and Gloerfelt and Margnat<sup>17</sup> performed an LES of a compressible turbulent boundary layer at three high speed Mach numbers. They predicted the acoustic radiation at observers within the computational domain and also with a Ffowcs Williams-Hawkings solver. These predictions showed excellent agreement but had a considerable computational cost.

Recently, Miller<sup>18</sup> developed the cross-spectral acoustic analogy (CSAA), which is capable of predicting the near-field cross-spectra of acoustic pressure from an arbitrary turbulent field in motion. When both observers are placed at the same spatial location the model predicts the auto-spectra of acoustic pressure. If the observers are at the same location and in the far-field, then the model reduces to the Lighthill acoustic analogy in the frequency domain. Recently, the CSAA was successfully applied to predict acoustic radiation from boundary layer turbulence without pressure gradients by Miller.<sup>19</sup> The model arguments were based on the similarity solutions of the turbulent boundary layer. The CSAA is the basis of this paper, and it requires knowledge of the statistics within the turbulent field, which is the turbulent boundary layer.

We now examine the model equation of Miller.<sup>19</sup> It was argued that by only retaining dominant terms of the Reynolds stress, approximating the length scales as proportional to the distance from the wall, only examining a differential volume element  $V$ , and approximating the coefficient matrix as  $A_{ijlm} \propto \bar{\rho}^2 (c_f \rho_\infty \rho_w^{-1} u_\infty^2)^2$ , the spectral density scales as

$$S \propto c_f^2 \bar{\rho}^2 \left( \frac{\rho_\infty}{\rho_w} \right)^2 l_{sx} l_{sy} l_{sz} \tau_s \left\{ \frac{\bar{u}^4 u_\infty^4}{c_\infty^4 r^2 l_{sx}^4} + \frac{\bar{u}^2 u_\infty^4}{c_\infty^2 r^4 l_{sx}^2} + \frac{u_\infty^4}{r^6} \right\} V, \quad (1)$$

where  $c$  is the speed of sound,  $c_f$  is the skin friction,  $l_{si}$  is the turbulent length scale in the direction  $i$ ,  $r$  is the propagation distance,  $S$  is the spectral density,  $u$  is the streamwise velocity component,  $V$  is the differential volume element,  $\rho$  is the density, and  $\tau_s$  is the turbulent time scale. Here, the terms in the brackets correspond to the far-field, mid-field, and near-field radiation. Effectively, the far-field term scales with  $\bar{u}^4 u_\infty^4$ , the mid-field term scales with  $\bar{u}^2 u_\infty^4$ , and the near-field term scales with  $u_\infty^4$ . Miller<sup>19</sup> assumed that the length scales are proportional to the compressible boundary layer thickness and that the observer is in the far-field. Using the definition of turbulent kinetic energy, using one-point turbulent scale estimation, and using simplified relations for the Reynolds stresses, a simplified scaling for the spectral density of acoustic pressure in the far-field from a turbulent boundary layer was proposed

$$S_{\text{far-field}} \propto \frac{1}{r^2} \frac{c_f^2}{c_\infty^4} \frac{\tau_s}{\delta} \left( \frac{\bar{\rho} \rho_\infty}{\rho_w} \right)^2 u_\infty^8 V, \quad (2)$$

where  $\delta$  is the boundary layer thickness. Here, the spectral density,  $S$ , scales as the eighth power of  $u_\infty$ , which is consistent with the theory of Lighthill for the scaling of noise from turbulence. The other arguments within Eqn. 2 are derived from basic boundary layer theory (see Schlichting<sup>5</sup> for details). Compressibility and temperature effects have the greatest impact on the density terms ( $\bar{\rho}$  and  $\rho_w$ ) within Eqn. 2. The spectral density scales with the eighth power of velocity, and the spectral density is most sensitive to this argument and is relatively less sensitive to the other arguments.

In this paper, the model for the spectral density of acoustic pressure is applied to the non-zero pressure gradient turbulent boundary layer. Unlike the previous approach, the model is now adapted and subsequently connected to steady RANS solutions of the non-zero pressure gradient turbulent boundary layer. Statistics of turbulence are now numerically computed using an algebraic Reynolds-stress closure. Both aerodynamic and aeroacoustic predictions are compared with theory and purely numerical predictions. The variation of the turbulent statistics and radiated noise are examined with respect to changes in the non-dimensional pressure gradient.

In the next section of this paper, the mathematical model and its connection to steady RANS solutions are shown. Implementation of the model is then discussed. Numerical solutions of the RANS equations for boundary layers and acoustic predictions based on the RANS solutions are then shown.

## Mathematical Theory

Predictions of the spectral density of acoustic pressure are conducted using the theory of Miller.<sup>19</sup> Here, the cross-spectral acoustic analogy is used, which is a statistical solution of the Navier-Stokes equations in the form of the Lighthill acoustic analogy. We retain the far-field term, as it was previously shown that the mid-field and near-field terms contribute very little acoustic energy within a subsonic turbulent boundary layer. It was shown that the spectral density of the acoustic pressure from a turbulent boundary layer with one particular form for the two-point cross-correlation of the equivalent source is

$$S(\mathbf{x}, \omega) = 4\pi^{-2} \int_{-\infty}^{\infty} \dots \int_{-\infty}^{\infty} \{A_{ijlm} l_{sy} l_{sz} F_t \mathcal{I}\} d\xi d\boldsymbol{\eta}, \quad (3)$$

where  $A_{ijlm}$  is a coefficient matrix,  $\xi$  is a vector between two sources in the axial direction, and  $\boldsymbol{\eta}$  is a vector from the origin to a point within the turbulent boundary layer. The far-field term is

$$F_t \approx \left[ \frac{1}{c_\infty^4 r r'} \right]. \quad (4)$$

The coefficient matrix  $A_{ijlm}$  is

$$A_{ijlm} \approx \mathcal{P}_f \bar{\rho} \overline{\rho' u_i u_j} \overline{u'_i u'_m}, \quad (5)$$

where  $\mathcal{P}_f$  is a constant coefficient. Within Eqn. 3,  $\mathcal{I}$  is

$$\mathcal{I} = \begin{cases} \frac{12\bar{u}^4}{l_{sx}^4} \frac{\pi^{1/2} l_{sx}}{2\bar{u}} \exp \left[ \frac{\bar{u}^2 - 2i\bar{u}(l_{sx} + 2\pi)\omega - l_{sx}^2 \omega^2 + \bar{u} \tanh[\alpha\xi](-2(\bar{u} + il_{sx}\omega) + \bar{u} \tanh[\alpha\xi])}{4\bar{u}^2} \right] \\ \times \left( \exp \left[ \frac{il_{sx}\omega \tanh[\alpha\xi]}{\bar{u}} \right] \operatorname{erfc} \left[ \frac{\bar{u} - il_{sx}\omega - \bar{u} \tanh[\alpha\xi]}{2\bar{u}} \right] + \exp \left[ \frac{il_{sx}\omega}{\bar{u}} \right] \operatorname{erfc} \left[ \frac{\bar{u} + il_{sx}\omega - \bar{u} \tanh[\alpha\xi]}{2\bar{u}} \right] \right) & \text{for } \xi \geq 0 \\ \text{and} \\ \frac{12\bar{u}^4}{l_{sx}^4} \frac{\pi^{1/2} l_{sx}}{2\bar{u}} \exp \left[ \frac{\bar{u}^2 - 2i\bar{u}(l_{sx} + 2\pi)\omega - l_{sx}^2 \omega^2 + \bar{u} \tanh[\alpha\xi](2(\bar{u} - il_{sx}\omega) + \bar{u} \tanh[\alpha\xi])}{4\bar{u}^2} \right] \\ \times \left( \operatorname{erfc} \left[ \frac{\bar{u} - il_{sx}\omega + \bar{u} \tanh[\alpha\xi]}{2\bar{u}} \right] + \exp \left[ \frac{il_{sx}\omega(1 + \tanh[\alpha\xi])}{\bar{u}} \right] \operatorname{erfc} \left[ \frac{\bar{u} + il_{sx}\omega + \bar{u} \tanh[\alpha\xi]}{2\bar{u}} \right] \right) & \text{for } \xi < 0. \end{cases} \quad (6)$$

The model integrations are based upon the mixed Gaussian-exponentially decaying model of the two-point cross-correlation of the equivalent source

$$R = \exp \left[ -\frac{(\xi - \bar{u}\tau)^2}{l_{sx}^2} \right] \exp \left[ -\frac{(1 - \tanh[\alpha|\xi|])|\xi - \bar{u}\tau|}{l_{sx}} \right] \exp \left[ -\frac{|\xi|}{l_{sx}} \right] \exp \left[ -\frac{|\eta|}{l_{sy}} \right] \exp \left[ -\frac{|\zeta|}{l_{sz}} \right], \quad (7)$$

where  $\alpha$  is a constant. We estimate the length scale within  $R$  by adopting the model of Efimtsov<sup>20</sup>

$$l_s = a_4 \delta \left[ \left( \frac{2\pi a_1 f}{u_c} \right)^2 + \frac{a_2^2}{\left( \frac{2\pi f \delta}{u_\tau} \right)^2 + \left( \frac{a_3}{a_3} \right)^2} \right]^{-\frac{1}{2}}, \quad (8)$$

where  $a_1 = 0.1$ ,  $a_2 = 72.8$ ,  $a_3 = 1.54$ , and  $a_4 = 6$ . The spanwise length scale uses an alternative set of coefficients, where  $a_1 = 0.1$ ,  $a_2 = 548$ ,  $a_3 = 13.5$ , and the other values of  $a$  remain the same.

The numerical evaluation of Eqn. 3 is complex. Equation 3 does not account for the interaction of acoustic radiation with the wall that bounds the flow. To account for the wall, we adopt the approach used by Powell,<sup>7</sup> who used the concept of the ‘mirror’ source. Equation 3 requires the knowledge of two observer positions, two source positions, and associated vectors dependent on the observer and source positions. Observer positions are restricted to  $y > \delta$ , where  $\delta$  is a function of  $x$ . Sources reside within the turbulent flow-field and are restricted to  $|y| \leq \delta$ , where the absolute value is due to the use of the mirror source concept. By examining Eqn. 3, it is evident that for every source position  $\mathbf{y}_1$  the vector  $\boldsymbol{\eta}$  is defined to include every possible source location  $\mathbf{y}_2$ . There is an acoustic propagation delay from the mirrored source. The source and its mirror share the same equivalent source. Numerical integration is performed using the CFD solution. Predictions are conducted iteratively for observer positions,  $\mathbf{x}$ , and frequencies,  $\omega$ . Spatial integrals of Eqn. 3 are evaluated numerically.

## Results

We examine non-zero pressure gradient turbulent boundary layers at four Mach numbers,  $\mathcal{M}_\infty = 0.30, 0.50, 0.70$ , and  $0.90$ . The reference length scale of the Reynolds number,  $\mathcal{R}e_x$ , is based on the unit distance from the leading edge,  $x_l = 1$  m. Estimations of relevant flow parameters of these four boundary layers with zero pressure gradient are shown in Table 1. These values are estimated with the theories presented by Schlichting.<sup>5</sup> We impose four non-dimensional pressure gradients through a source term of the momentum equation for each of the four  $\mathcal{M}_\infty$ . These non-dimensional pressure gradients are  $\partial\tilde{p}/\partial x = -0.02, -0.01, 0.01$ , and  $0.02$ . Four ambient Mach numbers and five non-dimensional pressure gradients are considered, therefore we examine 20 flow-fields and associated acoustic predictions. In Table 1,  $\tau_w$  is the wall shear stress,  $\delta$  is the boundary layer thickness,  $u_\tau$  is the friction velocity, and  $y^+$  is the distance corresponding to  $y^+ \approx 1$ . Unfortunately, a well developed theory is not available to estimate with accuracy these quantities with imposed pressure gradients. These numerically derived quantities will be presented in the next section, and finally aeroacoustic predictions will be presented.

## Aerodynamics

The meanflow and turbulent statistics of boundary layer flows with non-zero pressure gradients are obtained numerically with the Fully Unstructured Navier-Stokes (‘FUN3D’) CFD solver of NASA Langley Research Center. The FUN3D CFD solver calculates numerical solutions of the RANS equations closed by an appropriate turbulence model. Here, the RANS equations are closed by the Wilcox<sup>21</sup> Reynolds stress model

with compressibility corrections. With this choice of turbulence model, the full Reynolds stress tensor and meanflow are predicted. The solver performs between 10,000 and 40,000 iterations for each boundary layer flow examined. A Courant-Friedrichs-Lewy (CFL) time step ramping is performed for the first 250 iterations which linearly increases the CFL number from 0.5 to 25. The CFL number is held constant at 25 for the remaining iterations. Roe flux vector splitting without a flux limiter is used to discretize the equations. For full details of the solver see Biedron et al.<sup>22</sup>

A single computational domain is used for all numerical calculations. The computational domain is shown in Fig. 2, where the lines represent the connectivity between grid points. Though the solver is unstructured, a structured domain is used for the CFD calculations. The computational domain contains 249500 nodes and 124002 elements. The distance from the wall to the closest boundary point corresponds to  $y^+ \approx 0.2$  (highest value), thus the boundary layer flow is highly resolved. This point is initially found through an estimate of viscous layer thickness for the highest speed case. The distribution of grid points depends upon a hyperbolic tangent growth rate applied in the streamwise and cross-stream directions. The domain contains two planes separated by a distance of 0.01 m in the  $z$  direction. The use of a three-dimensional domain for two-dimensional flows is a requirement of the solver.

Multiple boundary conditions are imposed on the steady RANS equations closed by the Wilcox Reynolds stress model. The boundary conditions are consistent between simulations. Figure 2 shows the computational domain. Along the left boundary ( $x = -1$  m) a subsonic inflow is prescribed by imposing a total pressure and total temperature corresponding to the ambient Mach number. In these simulations, we primarily examine four subsonic Mach numbers of 0.30, 0.50, 0.70, and 0.90. The normalized values of total pressure,  $p_t$ , and total temperature,  $T_t$ , are shown in Table 2 for these four Mach numbers. At this inlet boundary condition the cross-stream velocity component is zero. At the right side of the grid ( $x = 3$  m), the static pressure is prescribed as the ambient pressure and is an outflow boundary condition. The upper boundary ( $y = 1$  m) is the Riemann invariant boundary condition. The lower boundary ( $y = 0$  m) is prescribed as a slip wall (streamwise velocity component can vary) in the range of  $x < 0$ , and in the range  $x \geq 0$  is a no-slip wall (velocity is zero). Finally, in the spanwise direction symmetry boundary conditions are imposed, which means that the spanwise mean velocity component is zero. For details of these boundary conditions see Biedron et al.<sup>22</sup>

The pressure gradient within the flow is imposed through an additional source term within the momentum equation. We enforce this source term explicitly by setting  $\partial\tilde{p}/\partial x$  to be a small non-zero number, where this quantity represents the non-dimensional pressure gradient. Here, the non-dimensional pressure gradient,  $\partial\tilde{p}/\partial x$ , is related to the actual pressure gradient through the factor  $\nu(\rho u_\infty^3)^{-1}\partial p/\partial x$ . The pressure gradient as a source term within the equations of motion will not exactly correspond to the pressure gradient within the flow-field as it represents a source term. The actual pressure gradient is calculated from the numerical solution.

We examine residual to quantify convergence of our numerical solver. Figure 3 shows the residual per iteration for the  $\mathcal{M}_\infty = 0.90$  and  $\partial\tilde{p}/\partial x = 0$  case. The  $y$ -axis is the residual of each unknown variable and the  $x$ -axis is the iteration number. We examine this case because the most iterations are performed for convergence. After the first few thousand iterations through iteration 35,000 continual reduction of the residual is obtained. After iteration 35,000, the residual has ceased reduction with increasing iteration. Generally, the residual of each unknown variable has increased by approximately five orders of magnitude from the initial condition. The initial condition of each simulation is the ambient Mach number and ambient pressure. For select cases, if the adverse pressure gradient is too large then the solution diverges. These divergent results are not examined further.

We now examine the numerical solution of the steady RANS equations. Contours of  $\mathcal{M} = \overline{u}c^{-1}$  are shown in Fig. 4. The  $y$ -axis is the cross-stream direction and the  $x$ -axis is the streamwise direction. The flow corresponds to  $\mathcal{M}_\infty = 0.50$  and  $\partial\tilde{p}/\partial x = 0$ . We derive our boundary layer profile statistics from the axial location of  $x_l = 1$ , where the turbulent boundary layer is well developed. These simulations assume that the profile is fully turbulent and starts evolving at the leading edge of the surface located at  $x = y = 0$ . Also, the contours of  $\mathcal{M}$  show that the flow in front of the plate is disturbed.

We have described and shown select numerical solutions of the steady RANS equations closed by the Wilcox Reynolds stress model. We derive flow statistics numerically from these solutions as it is not possible to find them readily through semi-empirical methods. Table 3 shows these numerically derived values for each solution that are dependent on  $\mathcal{M}_\infty$ ,  $\mathcal{R}e_x$ ,  $x_l$ , and  $\partial\tilde{p}/\partial x$ . These derived values are located at  $x_l = 1$ . Here,  $\tau_w$  is the wall shear stress,  $\delta$  is the boundary layer thickness,  $u_\tau$  is the friction velocity,  $y^+$  is the

distance from the wall to the first grid point, and  $\partial p/\partial x$  is the pressure gradient. It can be shown that the non-dimensional and numerically derived pressure gradient do not contain a linear relationship. The pressure gradient was prescribed as a momentum source. It is expected that as the adverse pressure gradient is increased then  $\delta$  will increase, which is observed in our numerical results.

The remaining part of this section examines quantitative comparisons of the numerical solutions with variation of the non-dimensional pressure gradient. We first examine the streamwise velocity component,  $u^+ = \bar{u}u_\tau^{-1}$ , relative to  $y^+$ . Figure 5 shows variation of  $u^+$  for four Mach numbers and for five non-dimensional pressure gradients. It is immediately apparent that at lower Mach numbers the effect of the same non-dimensional pressure gradient is much stronger than at higher Mach numbers. At  $\mathcal{M}_\infty = 0.3$ , the variation of  $u^+$  can be as much as 4 within the outer region of the boundary layer. Within the outer region of the boundary layer near  $y^+ \approx 100$ , there is minor divergence from the zero pressure gradient case. Almost no apparent variation is observed in the meanflow at  $\mathcal{M}_\infty = 0.90$ . Within the inner region of the boundary layer there is no variation, which shows that the inner region is invariant to non-dimensional pressure gradient at these Mach numbers.

The variation of  $\rho$  and  $T$  with  $\mathcal{M}_\infty$  and  $\partial\tilde{p}/\partial x$  is shown in Fig. 6. Both  $\rho$  and  $T$  are normalized by their respective ambient quantities,  $\rho_\infty$  and  $T_\infty$ . Large variations of  $\rho$  and  $T$  are observed relative to the zero pressure gradient case at low Mach numbers. As  $\mathcal{M}_\infty$  is increased, the variation of  $\rho$  and  $T$  is much more dramatic. At all Mach numbers, the variation of  $\partial\tilde{p}/\partial x$  causes changes of  $\rho$  and  $T$  throughout the entire boundary layer profile.

We now turn our attention to the variation of the turbulent statistics, in particular the Reynolds stress tensor components, with varying non-dimensional pressure gradient. Figure 7 shows the variation of  $\overline{u'u'}^{1/2}u_\tau^{-1}$  with  $\mathcal{M}_\infty$  and  $\partial\tilde{p}/\partial x$ . We present  $\overline{u'u'}^{1/2}u_\tau^{-1}$  relative to the baseline zero pressure gradient case. It is customary to collapse turbulent statistics for zero pressure gradient turbulent boundary layers by  $u_\tau$ , and we use the same approach here. Unlike some of the meanflow results the turbulent statistics are highly altered by the pressure gradient. At low Mach numbers the turbulent statistics are more sensitive to pressure gradient than at high Mach numbers. Large variations of the turbulent statistics are observed consistently near  $y^+ \approx 10$  and in the outer region. Note that each subfigure uses different ranges in the  $y$ -axis because of the large variations between Mach numbers.

The variation of the second and third diagonal components of the Reynolds stress tensor demonstrate similar trends. Figures 8 and 9 show  $\Delta\overline{v'v'}^{1/2}u_\tau^{-1}$  and  $\Delta\overline{w'w'}^{1/2}u_\tau^{-1}$  versus  $y^+$ . The trends of these two components are nearly identical except for their magnitudes. For example, compare Fig. 8 (a) with Fig. 9 (a), where the latter is approximately 60% in magnitude but the shape is nearly the same. The largest variations of the Reynolds stress components occur near low Mach numbers and there is considerably less variation at high Mach numbers.

We now examine the variation of off-diagonal Reynolds stress components. Figure 10 shows off-diagonal components  $\Delta\overline{u'v'}^{1/2}u_\tau^{-1}$ . Within the inner region of the boundary layer, the off-diagonal component increases in intensity and within the outer region it decreases in intensity. Near the edge of the boundary layer there are strong and narrow changes relative to the zero pressure gradient off-diagonal components.

Changes in Reynolds stresses and meanflow quantities are most apparent at low Mach numbers and changes are generally very small at high Mach numbers. Unfortunately, there is no known methodology to demonstrate similarity of the Reynolds stresses for non-zero pressure gradient boundary layers. In these numerical simulations, we have captured the variation of the meanflow and turbulent statistics with pressure gradient. These numerical results are now used as arguments in the model equation to predict the variation of acoustic radiation with non-zero pressure gradient.

## Aeroacoustics

We now use the developed acoustic analogy and numerically predicted turbulent statistics to conduct acoustic predictions. We first compare the present prediction with the model of Miller<sup>19</sup> and the LES solution of Gloerfelt and Berland<sup>16</sup> and Gloerfelt and Margnat.<sup>17</sup> Figure 11 shows these comparisons at three Mach numbers of 0.50, 0.70, and 0.90 for  $\partial\tilde{p}/\partial x = 0$ . The  $x$ -axis is frequency,  $f$ , and the  $y$ -axis is sound pressure level (SPL) per unit  $f$ . The two prediction approaches contain the same trends but there is variation especially near 30 kHz, where the spectrum starts to decay with increasing frequency. This is not unexpected as the model of Miller<sup>19</sup> used empirical models of the turbulent statistics, which are arguments of the acoustic analogy. Nonetheless, relative to the predictions of Gloerfelt and Margnat<sup>17</sup> we have some certainty that

the numerically derived turbulent statistics have been correctly incorporated into the prediction.

Figure 12 shows predictions of SPL per unit  $f$  for four Mach numbers at five non-dimensional pressure gradients. These flows and their associated properties are summarized in Table 3. At  $\mathcal{M}_\infty = 0.30$  the changes in acoustic radiation are extremely large. This is in contrast to the predictions at  $\mathcal{M}_\infty = 0.90$ , where a very small change in  $\Delta\text{dB}$  is apparent. These results are not unexpected as it was previously noted that the largest changes of turbulent statistics and meanflow properties occurred at low Mach numbers relative to high Mach numbers for constant non-dimensional pressure gradient. The clearest beneficial trend for noise reduction, especially at compressible Mach numbers, is that as pressure gradient becomes more favorable noise is reduced. Predicted spectra appear to not alter their overall shape but shift in frequency and amplitude, almost linearly, with changing pressure gradient.

## Conclusion

We showed numerical predictions of the changes in acoustic radiation from non-zero pressure gradient boundary layers for four subsonic Mach numbers and four non-dimensional pressure gradients. These comparisons are relative to the zero-pressure gradient boundary layer flow. The predictions are based upon an acoustic analogy that is connected to the turbulent statistics generated from a steady Reynolds-averaged Navier-Stokes solver closed by an algebraic Reynolds stress model. Predictions of the approach agreed with the previous analytical model and a well validated large eddy simulation. Also, the associated statistics for these cases is explored relative to the zero-pressure gradient boundary layer flow. It is shown that at low Mach numbers the statistics of turbulence, meanflow, and acoustic radiation are more so highly affected by pressure gradient relative to high Mach number subsonic flows. Small negative incremental steps in non-dimensional pressure gradient produce lower energy acoustic power spectra. The spectra shift to lower frequencies and sound pressure levels with favorable pressure gradients. Development of composite meanflow profiles and similarity of turbulent statistics with pressure gradient would allow a fully statistical model to be developed that does not rely on numerical simulation.

## References

- <sup>1</sup>Prandtl, L., "On Fluid Motion with Very Small Friction," *Heidelberg Mathematical Congress*, 1904.
- <sup>2</sup>Kovaszny, L. S. G., "The Turbulent Boundary Layer," *Annual Review of Fluid Mech.*, Vol. 2, No. 1, 1970, pp. 95–112. doi:[10.1146/annurev.fl.02.010170.000523](https://doi.org/10.1146/annurev.fl.02.010170.000523).
- <sup>3</sup>Kline, S. J., Reynolds, W. C., Schraub, F. A., and Runstadler, P. W., "The Structure of Turbulent Boundary Layers," *Journal of Fluid Mechanics*, Vol. 30, No. 4, 1967, pp. 741–773. doi:[10.1017/s0022112067001740](https://doi.org/10.1017/s0022112067001740).
- <sup>4</sup>Eichelbrenner, E. A., "Three-Dimensional Boundary Layers," *Annual Review of Fluid Mech.*, Vol. 5, No. 1, 1973, pp. 339–360. doi:[10.1146/annurev.fl.05.010173.002011](https://doi.org/10.1146/annurev.fl.05.010173.002011).
- <sup>5</sup>Schlichting, H. and Gersten, K., "Boundary-Layer Theory," *Springer*, 2000.
- <sup>6</sup>Castillo, L., "Similarity Analysis of Turbulent Boundary Layers," *State University of New York at Buffalo, Ph.D. Dissertation*, 1977.
- <sup>7</sup>Powell, A., "Aerodynamic Noise and the Plane Boundary," *Journal of the Acoustical Society of America*, Vol. 32, No. 8, 1960, pp. 982–990. doi:[10.1121/1.1908347](https://doi.org/10.1121/1.1908347).
- <sup>8</sup>Naka, Y., Stanislas, M., Foucaut, J. M., Coudert, S., Laval, J. P., and Obi, S., "Space-Time Pressure-Velocity Correlations in a Turbulent Boundary Layer," *Journal of Fluid Mechanics*, Vol. 771, 2015, pp. 624–675. doi:[10.1017/jfm.2015.158](https://doi.org/10.1017/jfm.2015.158).
- <sup>9</sup>Ffowcs Williams, J. E., "Sound Radiation from Turbulent Boundary Layers Formed on Compliant Surfaces," *Journal of Fluid Mechanics*, Vol. 22, No. 2, 1965, pp. 347–358. doi:[10.1017/s0022112065000794](https://doi.org/10.1017/s0022112065000794).
- <sup>10</sup>Ffowcs Williams, J. E., "The Acoustics of Turbulence Near Sound-Absorbent Liners," *Journal of Fluid Mechanics*, Vol. 51, No. 4, 1972, pp. 737–749. doi:[10.1017/s0022112072001338](https://doi.org/10.1017/s0022112072001338).
- <sup>11</sup>Ffowcs Williams, J. E. and Purshouse, M., "A Vortex Sheet Modelling of Boundary-Layer Noise," *Journal of Fluid Mechanics*, Vol. 113, 1981, pp. 187–220. doi:[10.1017/s0022112081003455](https://doi.org/10.1017/s0022112081003455).
- <sup>12</sup>Howe, M. S., "Surface Pressures and Sound Produced by Turbulent Flow Over Smooth and Rough Walls," *Journal of the Acoustical Society of America*, Vol. 90, No. 2, 1991, pp. 1041–1047. doi:[10.1121/1.402292](https://doi.org/10.1121/1.402292).
- <sup>13</sup>Glegg, S., Devenport, W., Grissom, D., and Smith, B., "Rough Wall Boundary Layer Noise: Theoretical Predictions," *13th AIAA/CEAS Aeroacoustics Conference (28th AIAA Aeroacoustics Conference)*, *AIAA Paper 2007-3417*, 2004. doi:[10.2514/6.2007-3417](https://doi.org/10.2514/6.2007-3417).
- <sup>14</sup>Hu, Z., Morfey, C., and Sandham, N. D., "Sound Radiation in Turbulent Channel Flows," *Journal of Fluid Mechanics*, Vol. 475, 2003. doi:[10.1017/s002211200200277x](https://doi.org/10.1017/s002211200200277x).
- <sup>15</sup>Hu, Z., Morfey, C., and Sandham, N. D., "Sound Radiation from a Turbulent Boundary Layer," *Physics of Fluids*, Vol. 18, No. 9, 2006, pp. 1–4. doi:[10.1063/1.2337733](https://doi.org/10.1063/1.2337733).
- <sup>16</sup>Gloerfelt, X. and Berland, G., "Turbulent Boundary-Layer Noise: Direct Radiation at Mach Number 0.5," *Journal of Fluid Mechanics*, Vol. 723, 2013, pp. 318–351. doi:[10.1017/jfm.2013.134](https://doi.org/10.1017/jfm.2013.134).

<sup>17</sup>Gloerfelt, X. and Margnat, F., “Effect of Mach number on Boundary Layer Noise,” *20th AIAA/CEAS Aeroacoustics Conference, AIAA Paper 2014-3291*, 2014. doi:[10.2514/6.2014-3291](https://doi.org/10.2514/6.2014-3291).

<sup>18</sup>Miller, S. A. E., “Prediction of Near-Field Jet Cross Spectra,” *AIAA Journal*, Vol. 53, No. 8, 2015, pp. 2130–2150. doi:[10.2514/1.J053614](https://doi.org/10.2514/1.J053614).

<sup>19</sup>Miller, S. A. E., “Prediction of Turbulent Boundary-Layer Noise,” *AIAA Journal*, 2017. doi:[10.2514/1.J055087](https://doi.org/10.2514/1.J055087).

<sup>20</sup>Efmntsov, B. M., “Characteristics of the Field of Turbulent Wall Pressure Fluctuations at Large Reynolds Numbers,” *Soviet Physics Acoustics*, Vol. 28, No. 4, 1982, pp. 289–292.

<sup>21</sup>Wilcox, D. C., “Turbulence Modeling for CFD,” *DCW Industries, 3rd edition, La Canada, CA*, 2006.

<sup>22</sup>Biedron, R. T., Carlson, J. R., Derlaga, J. M., Gnoffo, P. A., Hammond, D. P., Jones, W. T., Kleb, B., Lee-Rausch, E. M., Nielsen, E. J., Park, M. A., Rumsey, C. L., Thomas, J. L., and Wood, W. A., “FUN3D Manual: 12.9,” *NASA TM 2016-219012*, 2016.

<sup>23</sup>Lee, J. H., Kwon, Y. S., Monty, J. P., and Hutchins, N., “Tow-Tank Investigation of the Developing Zero-Pressure-Gradient Turbulent Boundary Layer,” *18th Australasian Fluid Mechanics Conference*, 2012.

## Tables

**Table 1. Theory based flow conditions.**

$\mathcal{M}_\infty$	$Re_x$	$x_l$ [m]	$\tau_w$ [Pa]	$\delta$ [m]	$u_\tau$ [ms <sup>-1</sup> ]	$y^+$ Distance [m]
0.30	$6.818 \times 10^6$	1	20.43	$3.073 \times 10^{-2}$	4.117	$3.667 \times 10^{-6}$
0.50	$1.136 \times 10^7$	1	53.24	$2.976 \times 10^{-2}$	6.646	$2.271 \times 10^{-6}$
0.70	$1.591 \times 10^7$	1	100.2	$2.916 \times 10^{-2}$	9.116	$1.656 \times 10^{-6}$
0.90	$2.045 \times 10^7$	1	160.7	$2.872 \times 10^{-2}$	11.55	$1.307 \times 10^{-6}$

**Table 2. Steady RANS inlet boundary conditions.**

$\mathcal{M}_\infty$	$p_t p_\infty^{-1}$	$T_t T_\infty^{-1}$
0.30	1.06443	1.01800
0.50	1.18621	1.05000
0.70	1.38710	1.09800
0.90	1.69130	1.16200

**Table 3. Numerically derived flow properties.**

$\mathcal{M}_\infty$	$Re_x$	$x_l$ [m]	$\tau_w$ [Pa]	$\delta$ [m]	$u_\tau$ [ms <sup>-1</sup> ]	$y^+$ Distance [m]	$\partial\bar{p}/\partial x$	$\partial p/\partial x$ [Pa m <sup>-1</sup> ]
0.30	$6.818 \times 10^6$	1	12.512	$7.792 \times 10^{-3}$	3.223	$4.683 \times 10^{-6}$	0	-12
0.30	$6.818 \times 10^6$	1	21.812	$2.709 \times 10^{-3}$	4.282	$3.525 \times 10^{-6}$	0.01	336
0.30	$6.818 \times 10^6$	1	30.531	$5.957 \times 10^{-3}$	5.089	$2.966 \times 10^{-6}$	0.02	346
0.30	$6.818 \times 10^6$	1	2.7360	$1.170 \times 10^{-2}$	1.493	$1.010 \times 10^{-5}$	-0.01	-770
0.30	$6.818 \times 10^6$	1	2.4245	$9.896 \times 10^{-5}$	1.401	$1.077 \times 10^{-5}$	-0.02	-2855
0.50	$1.136 \times 10^7$	1	36.468	$4.388 \times 10^{-3}$	5.528	$2.730 \times 10^{-6}$	0	-21
0.50	$1.136 \times 10^7$	1	45.299	$4.314 \times 10^{-3}$	6.204	$2.433 \times 10^{-6}$	0.01	272
0.50	$1.136 \times 10^7$	1	53.394	$4.250 \times 10^{-3}$	6.771	$2.229 \times 10^{-6}$	0.02	450
0.50	$1.136 \times 10^7$	1	30.283	$4.499 \times 10^{-3}$	5.039	$2.995 \times 10^{-6}$	-0.01	-483
0.50	$1.136 \times 10^7$	1	22.445	$4.762 \times 10^{-3}$	4.322	$3.492 \times 10^{-6}$	-0.02	-828
0.70	$1.591 \times 10^7$	1	71.474	$2.624 \times 10^{-3}$	7.853	$1.923 \times 10^{-6}$	0	-29
0.70	$1.591 \times 10^7$	1	79.688	$2.677 \times 10^{-3}$	8.357	$1.807 \times 10^{-6}$	0.01	149
0.70	$1.591 \times 10^7$	1	87.488	$2.721 \times 10^{-3}$	8.816	$1.713 \times 10^{-6}$	0.02	251
0.70	$1.591 \times 10^7$	1	66.807	$2.583 \times 10^{-3}$	7.622	$1.981 \times 10^{-6}$	-0.01	-756
0.70	$1.591 \times 10^7$	1	61.686	$2.558 \times 10^{-3}$	7.341	$2.057 \times 10^{-6}$	-0.02	-1250
0.90	$2.045 \times 10^7$	1	117.434	$1.976 \times 10^{-3}$	10.398	$1.452 \times 10^{-6}$	0	-26
0.90	$2.045 \times 10^7$	1	124.998	$1.990 \times 10^{-3}$	10.823	$1.395 \times 10^{-6}$	0.01	13
0.90	$2.045 \times 10^7$	1	133.133	$7.066 \times 10^{-4}$	11.394	$1.326 \times 10^{-6}$	0.02	939
0.90	$2.045 \times 10^7$	1	112.932	$1.968 \times 10^{-3}$	10.247	$1.473 \times 10^{-6}$	-0.01	-1288
0.90	$2.045 \times 10^7$	1	108.354	$1.963 \times 10^{-3}$	10.084	$1.497 \times 10^{-6}$	-0.02	-2352

## Figures

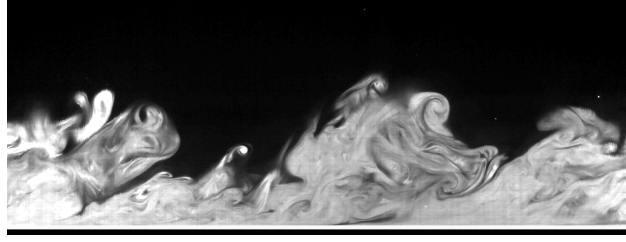


Figure 1. Photograph of a high Reynolds number turbulent boundary layer, moving from left to right, which is illuminated by laser induced fluorescence. The photograph is courtesy of Lee et al.<sup>23</sup>

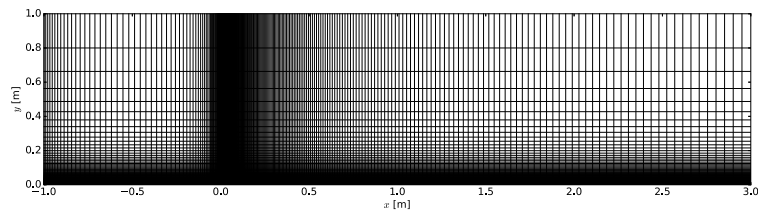


Figure 2. The computational domain.

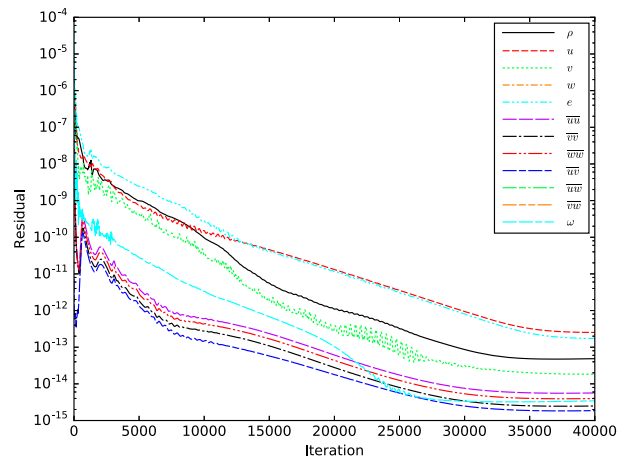


Figure 3. Variation of residual of field-variables for  $\mathcal{M}_\infty = 0.90$  and  $\partial\bar{p}/\partial x = 0$ .

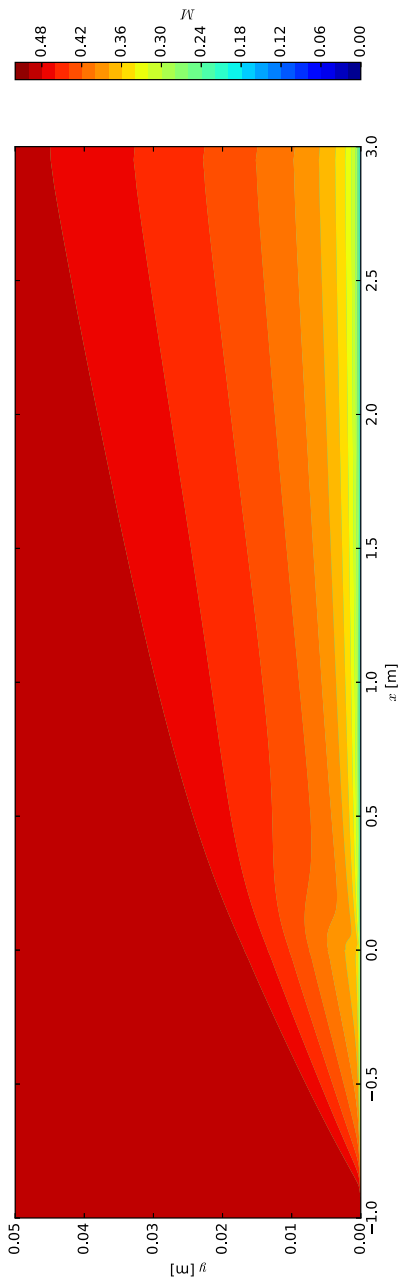


Figure 4. Contours of  $M$  for  $M_\infty = 0.50$  and  $\partial \bar{p} / \partial x = 0$ .

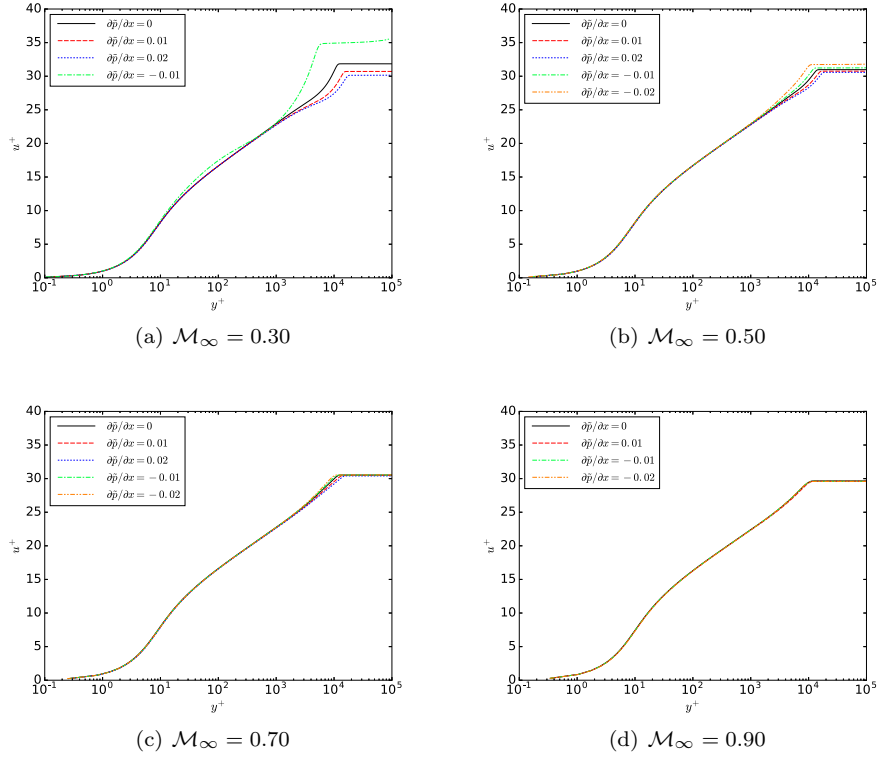


Figure 5. Variation of  $u^+$  in inner coordinates as function of  $M_\infty$  and  $\partial \bar{p} / \partial x$ .

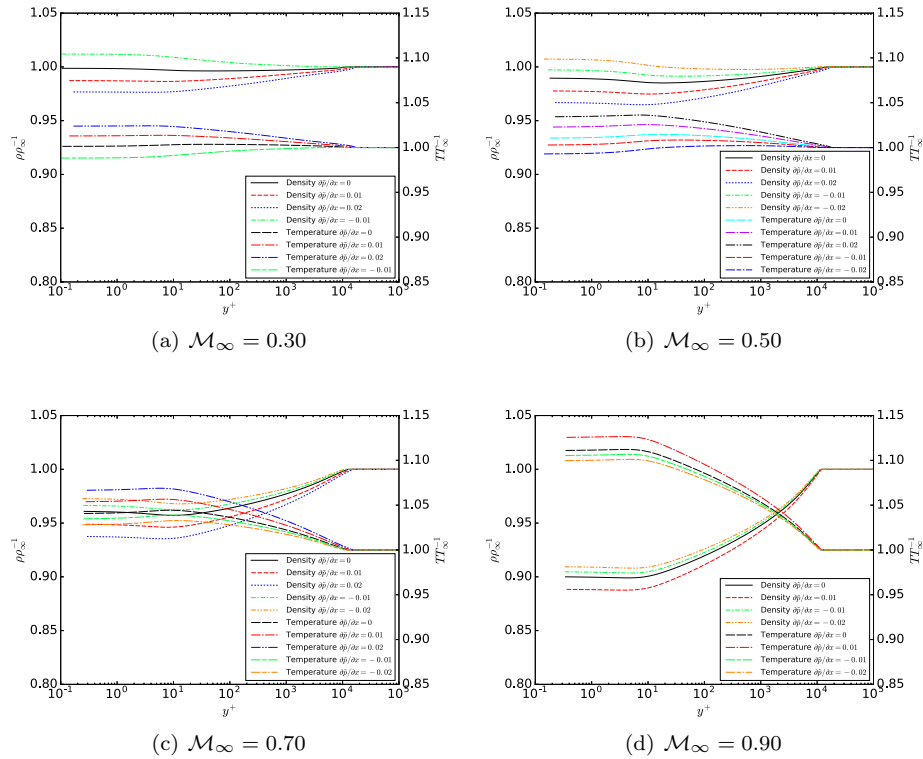
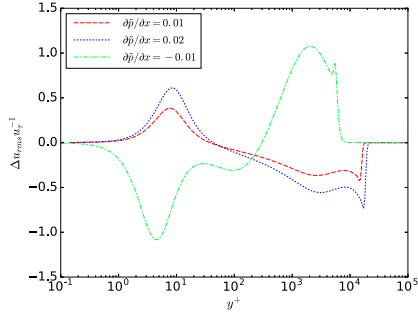
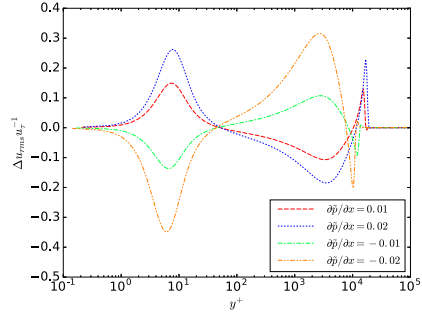


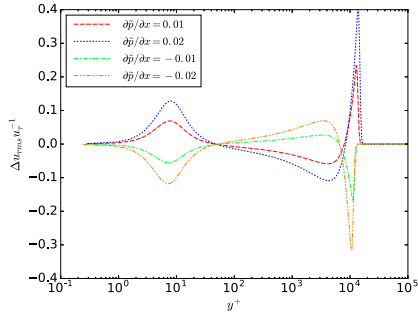
Figure 6. Variation of  $\rho$  and  $T$  in inner inner coordinates for various  $M_\infty$ .



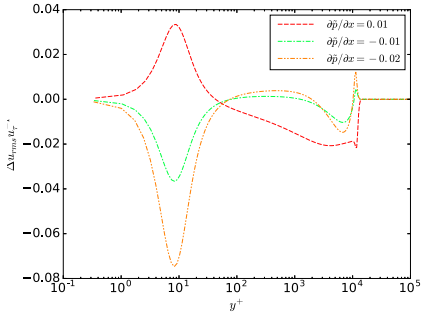
(a)  $M_\infty = 0.30$



(b)  $M_\infty = 0.50$

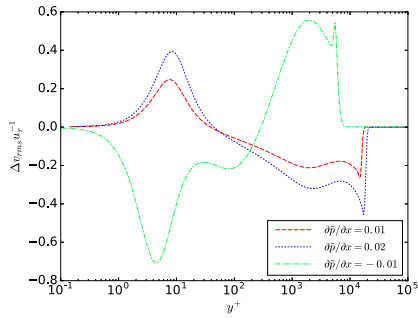


(c)  $M_\infty = 0.70$

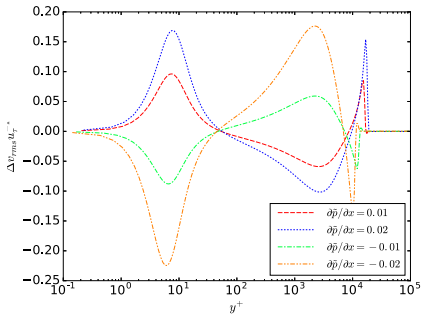


(d)  $M_\infty = 0.90$

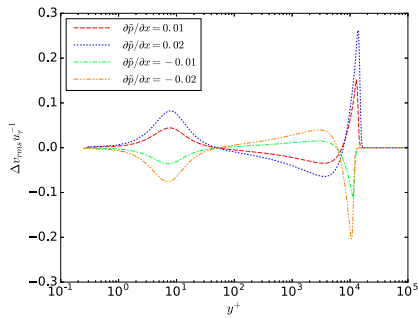
Figure 7. Normalized variation of  $u_{rms}$  in inner coordinates.



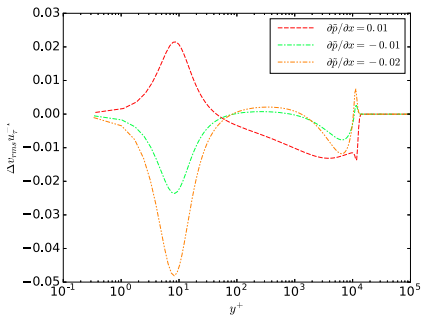
(a)  $M_\infty = 0.30$



(b)  $M_\infty = 0.50$



(c)  $M_\infty = 0.70$



(d)  $M_\infty = 0.90$

Figure 8. Normalized variation of  $v_{rms}$  in inner coordinates.

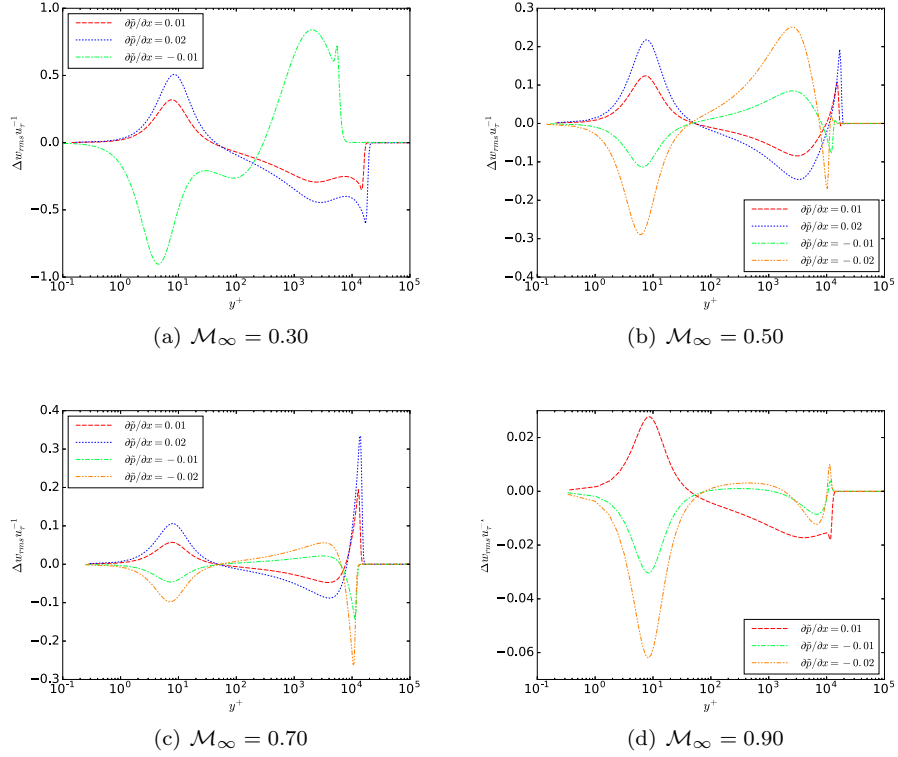


Figure 9. Normalized variation of  $w_{rms}$  in inner coordinates.

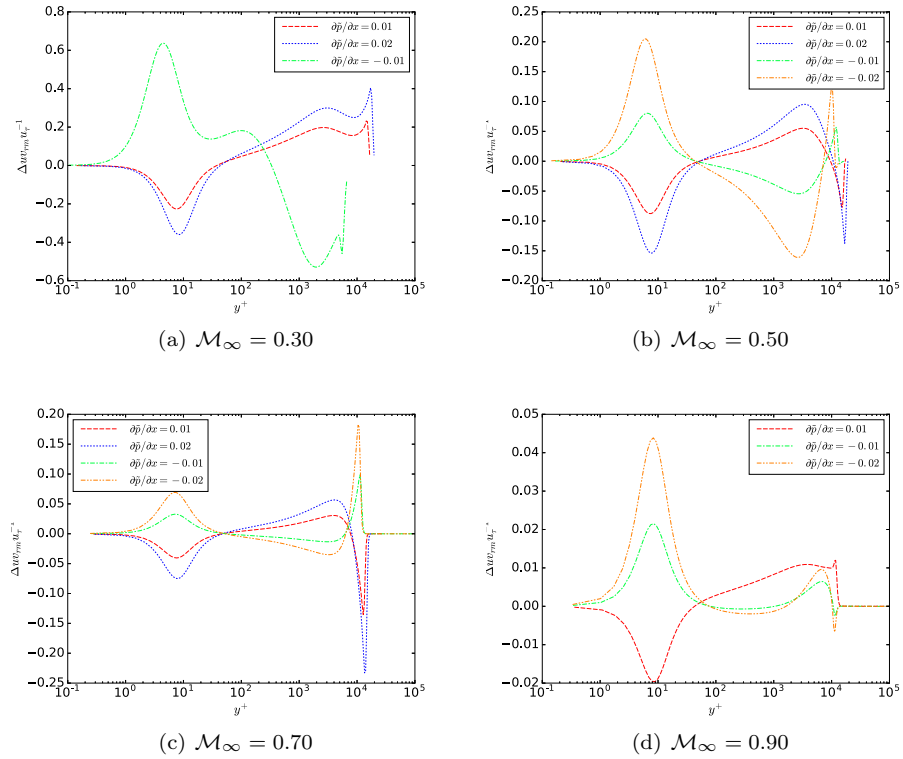


Figure 10. Normalized variation of the root mean of  $uv$  in inner coordinates.

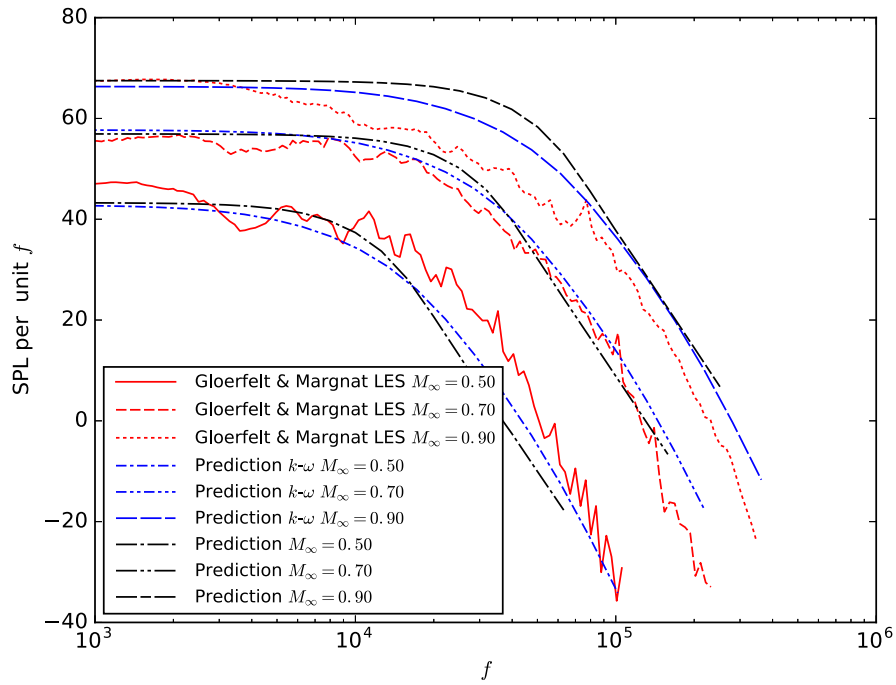


Figure 11. Comparison of the newly developed prediction approach with the predictions of Miller and the LES predictions of Gloerfelt and Margnat.

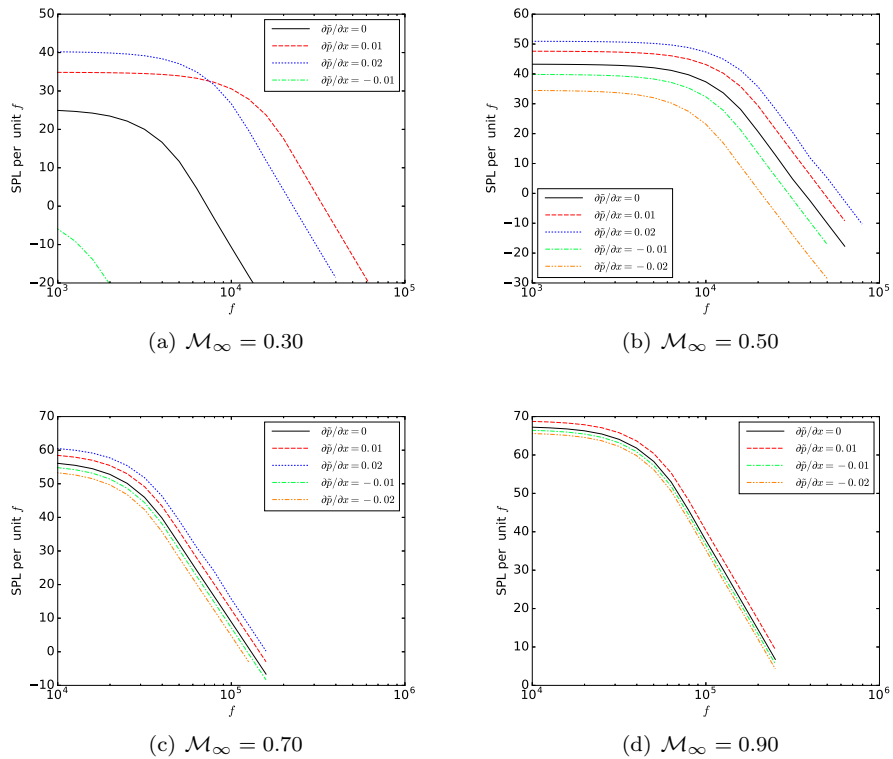


Figure 12. Predictions of SPL per unit  $f$  with various  $M_\infty$  and  $\partial \bar{p} / \partial x$ .